NUMERICAL INVESTIGATION OF THE EFFECT OF PROJECTILE MASS AND DROP HEIGHT FROM WATER SURFACE ON PINCH-OFF TIME AND DEPTH

Mohammad Hossein Taghizadeh Valdi
Department of Civil Engineering, Isfahan (Khorasgan) Branch, Islamic Azad University, Isfahan, Iran.

Mohammad Reza Atrechian
Department of Civil Engineering, Zanjan Branch, Islamic Azad University, Zanjan, Iran., m.atrechian@iauz.ac.ir

NUMERICAL INVESTIGATION OF THE EFFECT OF PROJECTILE MASS AND DROP HEIGHT FROM WATER SURFACE ON PINCH-OFF TIME AND DEPTH

Mohammad Hossein Taghizadeh Valdi[1], Mohammad Reza Atrechian[2],
Ata Jafary Shalkoohy[3], and Elham Chavoshi[1]

ABSTRACT

In this study, the water entry problem of spherical projectile was numerically simulated by the commercial finite element code Abaqus, and the effect of increasing the projectile mass and drop height from free water surface on deepwater displacement, viscous dissipation energy as well as pinch-off time and depth was investigated. An explicit dynamic analysis method was employed to model fluid-structure interactions using a Coupled Eulerian-Lagrangian (CEL) formulation. Accuracy of the numerical methodology and employed algorithm was verified by comparing the numerical results with the available experimental observations including shape of the air cavity and pinch-off time and depth. The results reveal that increasing the spherical projectile mass and drop height from free water surface up to the critical height leads to a decrease in its submersion time from the moment of water surface impact, until it reaches the model bed and greater than the critical drop height has a reverse effect on projectile impact velocity. The pinch-off time is a very weak function of projectile mass and impact velocity on water surface, but the pinch-off depth significantly increases along with increased mass and impact velocity of projectile. Additionally, the projectile mass has a subtle effect on viscous dissipation energy, while increasing the drop height of the projectile above the free water surface leads to a significant decrease in viscous

dissipation energy.

I. INTRODUCTION

The study of the hydrodynamic impact of solid bodies with water surface has been of particular importance for marine structures designers for more than 80 years. Accurate prediction of water impact forces has particular importance in design of marine structures and projectiles employed in dynamic compaction of seabed. The water entry of projectiles can be categorized by whether a cavity is formed or not. Based on cavity creation mechanism, the cavity-forming cases are classified into two main categories: air entrainment and supercavitation. The main feature of the air entraining cavity formation is an air cavity extending from the projectile up to the level of the undisturbed free surface and a splash crown that is ejected upward. On the other hand, projectiles traveling at high velocities in water can vaporize local pockets of liquid. Actually, cavitation occurs in a liquid when the local static pressure becomes less than the liquid vapor pressure. More details on the specifications of each group can be found in the recent review paper by Truscott et al. (2014). The studies on the water entry problem can also be classified based on the method of analysis. They can be divided into three main categories: experimental studies, analytical solutions and numerical simulations. What follows is a brief review on each category.

1. Experimental Studies

In the last three decades, many researchers have addressed the water entry problem using various methods. Worthington and Cole (1897) presented an initial image of water impact cavity and splash by using single-spark photography. Worthington (1908) studied water entry problem of vertical spherical objects. Watanabe (1930, 1934) investigated the impact of cones upon water and performed a quantitative experimental work to measure the impact force on an object upon entering water. Gilbarg and Andersok (1948) investigated the effect of surface tension, solid velocity, and atmospheric pressure on the entry

of spheres into water. May (1948, 1951, 1952) published three important papers to try to find the drag coefficient and the scaling relationship in water entry of blunt solid bodies by considering the Reynolds and Froude numbers. Moghisi and Squire (1981) experimentally estimated the initial force of the impact on a sphere striking a liquid surface. Experimental investigations were continued by New et al. (1993) studying water impact of prismatic bodies with different noses. Using the finite element method, Anghileri and Spizzica (1995) assessed the vertical impact of a rigid sphere to the water surface, and conducted some tests to calculate sphere acceleration change at the time of strike to validate the employed numerical method. Lee et al. (1997) investigated the effect of surface tension and Bernoulli pressure on the splash closure. Engle and Lewis (2003) observed a good agreement between the results of hydrodynamic forces resulting from the vertical impact of rigid body upon water surface that were computed with several different methods such as 2D boundary element and finite element modelling, and experimental analytical results of Wagner (1932) and Chaung (1966). Using experimental and theoretical methods, Aristoff et al. (2010) surveyed vertical water entry of various density spheres. They computed the time and depth of bubble separation and the sphere penetration depth at the time of separation by means of experimental observations. Techet and Truscott (2011) presented an experimental study of the trajectories, forces, and cavity formation behind spinning hydrophobic and hydrophilic spheres. Goharzadeh and Molki (2012) developed an experimental setup for characterizing the vertical motion of a horizontal circular cylinder through a free surface.

2. Analytical Solutions

The first published study on analytical determination of water impact force dates back to 1929. Using simple principles such as momentum conservation and the concept of added mass, Von Karman (1929) computed the impact forces exerted on floats when entering water. Most studies conducted prior to 1959 have focused on expanding the physical images presented by Von Karman, an extensive review of which has been offered by Szebehely (1959). Miloh (1991) investigated the water entry problem of rigid spheres. He expanded an analytical solution to determine the impact forces of angled water entry of spheres. In the same year, Howison et al. (1991) extended the previous analytical results of 2D body's impact on water surface. Aristoff and Bush (2009) studied water entry of small hydrophobic spheres and vertical cylinders. Tassin et al. (2013) studied the water entry problem for two-dimensional bodies through an analytical model and the capabilities of the proposed analytical model were investigated via a computational fluid dynamics (CFD) simulation.

3. Numerical Simulations

Glowinski et al. (1999) developed a new Lagrange-multiplier for the numerical simulation of fluid-solid interaction. Park et al. (2003) presented a numerical method to compute the impact and ricochet forces of high velocity water-entry bodies. In the same year, Battistin and Iafrati (2003) conducted a numerical analysis

of vertical water entry of a symmetrical or asymmetrical 2D body with arbitrary shape. Korobkin and Ohkusu (2004) studied the Hydro-elastic coupling of finite element model with regard to water entry problem. Kleefsman et al. (2005) conducted a 2D study of the water entry problem of wedge shaped and cylindrical bodies. Zhu et al. (2006) numerically investigated the water entry of a horizontal circular cylinder using the Constrained Interpolation Profile (CIP) method. Kim et al. (2007) analyzed the water entry problem of symmetrical bodies using particle hydrodynamic method. Yang and Qiu (2007) studied the water entry problem of symmetrical and asymmetrical blades with very entry low angle (smaller than 3 and 4 degrees). During the same year, Fairlie-Clarke and Tveitnes (2007) investigated the constant velocity impact of wedge shaped cross sections with water surface. Hafsia et al. (2009) presented two-dimensional numerical simulations of the water entry and exit of horizontal circular cylinders at a constant velocity. Mirzaii and Passandideh-Fard (2012) presented a 2D numerical algorithm for simulating the fluid-solid interactions in presence of a free-surface. Yang and Qiu (2012) conducted a numerical analysis on the forces imposed on projectile at the time of entering water. Employing boundary element method, Wu (2012) simulated the phenomenon of wedge impact on water surface. Ahmadzadeh et al. (2014) conducted a numerical simulation of the free impact of a sphere on water surface by means of the Coupled Eulerian-Lagrangian method. Nguyen et al. (2014) studied the water impact of various 3D geometries, namely a hemisphere, two cones and a free falling wedge, with an implicit algorithm based on a dual-time pseudo-compressibility method. S. Kim and N. Kim (2015) performed integrated dynamics modeling of supercavitating vehicles and established the 6-DOF equations by defining the hydrodynamic forces and moments. Nguyen et al. (2016) also used a moving Chimera grid method to predict the real-time motion of water entry bodies by combining the 6-DOF rigid body motion model and the numerical calculation of the multiphase flow field, by which the coupled effect of supercavity and moving body can be obtained. Mirzaei et al. (2016) held the idea that the existing planing force models weaken the nonlinear interaction among the solid, liquid, and gaseous phases and are often too simple and therefore inaccurate. Iranmanesh and Passandideh-Fard (2017) developed a 3D numerical scheme to simulate the hydrodynamics of a circular cylinder entering water horizontally. They investigated the effects of different parameters namely diameter, length, density ratio, and cylinder impact velocity on the non-dimensional depth. Taghizadeh-Valdi et al. (2018) numerically simulated the water entry problem of three-dimensional pounders with different geometric shapes of cube, cylinder, sphere, pyramid, and cone to dynamic compaction of seabed. They investigated the effect of pounder shape on deepwater displacement and velocity. This study set out to investigate the capability of the Coupled Eulerian-Lagrangian (CEL) method to simulate the water entry problem of bodies using the Abaqus software and accuracy of the algorithm used to solve these problems. Because the CFD method is mostly used in solving the fluid-structure interaction problems, while CEL method is also a power-

ful tool for solving these problems, which is available in Abaqus software, it can effectively model the fluid-structure interactions in a simpler manner with respect to the common CFD methods.

In this study, the water entry problem of spherical projectile was numerically simulated by the commercial finite element code Abaqus 6.14-2. An explicit dynamic analysis method was employed to model the fluid-structure interactions using a Coupled Eulerian-Lagrangian (CEL) formulation. The method can effectively model the fluid-structure interactions in a simpler manner with respect to the common CFD methods. The spherical projectile was regarded as a rigid body and its mesh was created in Lagrangian form. The water was also considered as a compressible and viscous fluid and its mesh was created in Eulerian form. Before simulating the water entry problem of the spherical projectile, accuracy of the numerical methodology and employed algorithm was verified by comparing the numerical results with the available experimental observations, and the effect of increasing the projectile mass and drop height from water surface on deepwater displacement, viscous dissipation energy and pinch-off time and depth and was investigated. Then, the critical drop height of the projectile which is indicative of its maximum velocity in water depth was determined.

II. COUPLED EULERIAN-LAGRANGIAN (CEL) METHOD

In a traditional Lagrangian, analysis nodes are fixed within the material, and elements deform as the material deforms. Lagrangian elements are always 100% full of a single material, so the material boundary coincides with an element boundary. By contrast, in an Eulerian analysis, nodes are fixed in space, and material flows through elements that do not deform. Eulerian elements may not always be 100% full of material; many may be partially or completely void. The Eulerian material boundary must, therefore, be computed during each time increment and generally does not correspond to an element boundary. The Eulerian mesh is typically a simple rectangular grid of elements constructed to extend well beyond the Eulerian material boundaries, giving the material space in which to move and deform. If any Eulerian material moves outside the Eulerian mesh, it is lost from the simulation. Eulerian material can interact with Lagrangian elements through Eulerian-Lagrangian contact; simulations that include this type of contact are often referred to as Coupled Eulerian-Lagrangian (CEL) analysis (Ahmadzadeh et al., 2014). This is a powerful tool that allows to solve multi-phased problems including fluid structure contact. In the Coupled Eulerian-Lagrangian method, the calculated pressures and stresses in the Eulerian mesh are applied on the Lagrangian cells as external loads. The Lagrangian mesh motion, however, acts as a boundary condition on the flow of material in the Eulerian meshes (Erfanian et al., 2015).

The Eulerian is implemented in Abaqus software using the volume-of-fluid (VOF) method. In CEL method, the Eulerian material is tracked as it flows through the mesh by computing its Eulerian volume fraction (EVF). Each Eulerian element is designated a percentage, which represents the portion of that element filled with a material. If an Eulerian element is completely filled with a material, its EVF is 1; if there is no material in the element, its EVF is 0. The Eulerian elements may simultaneously contain more than one material. If the sum of all material volume fractions in an element is less than one, the remainder of the element is automatically filled with "void" material which has neither mass nor strength. Contact between Eulerian materials and Lagrangian materials is enforced using a general contact that is based on a penalty contact method. The Lagrangian elements can move through the Eulerian mesh without resistance until they encounter an Eulerian element filled with material (EVF ≠ 0). The attractiveness of this method is that the fluid is modeled in an Eulerian frame while the projectile can still be modeled in a Lagrangian frame as is typical for solid mechanics applications. Specifically, in CEL, the governing equation of the solid uses the conservation of momentum, while the governing equation for the fluid uses a general form of Navier-Stokes. A CEL method that attempts to capture the advantages both of the Lagrangian and the Eulerian method is implemented in Abaqus (Taghizadeh-Valdi et al., 2018).

1. Coupling Procedure

The contact algorithm in CEL follow the Penalty contact method. Contact condition is dependent on the penetration of the Lagrangian description (Structure) onto the Eulerian description (Fluid). The interaction occurs between the Lagrangian and Eulerian nodes, which are termed as slave and master nodes, respectively. The penetration depth of the slave node is calculated from the relative velocity between the slave node and the master node and is sequentially updated at each time step as (Shirole et al., 2017):

$$d^{n+1} = d^n + \left[V_s^{n+\frac{1}{2}} - V_m^{n+\frac{1}{2}} \right] \cdot \Delta t \qquad (1)$$

where V_s and V_m specifies the slave and master node velocities, respectively, while d is the penetration depth at each time increment. The superscript (n) refers to the increment number and $\left(n+\frac{1}{2} \right)$ points to mid increment. The penalty coupling method is analogous to the behaviour of spring system. The penalty forces are proportional to the penetration depth and spring stiffness.

2. Time Integration Scheme

The CEL method implemented in Abaqus/Explicit uses an explicit time integration scheme. The discretised equation of motion can be written in the form (Shirole et al., 2017):

$$\ddot{u} = M^{-1} \cdot \left(F^{ext} - F^{int} \right) \qquad (2)$$

where M is the mass matrix, $\ddot{u}$ is the nodal acceleration vector with the superposed dot a material derivative of the nodal displacement u with respect to time, F^{ext} and F^{int} are the external

and internal nodal force vectors, respectively. Eq. (2) is integrated explicitly using central difference integration as follows:

$$\dot{u}^{\left(n+\frac{1}{2}\right)} = \dot{u}^{\left(n-\frac{1}{2}\right)} + \frac{\Delta t^{(n+1)} + \Delta t^{(n)}}{2} \cdot \ddot{u} \qquad (3)$$

$$u^{(n+1)} = u^{(n)} + \Delta t^{(n+1)} \cdot \dot{u}^{\left(n+\frac{1}{2}\right)} \qquad (4)$$

where $\dot{u}$ is velocity, u is displacement and Δt is the time increment. The superscript (i) refers to the increment number while $\left(n-\frac{1}{2}\right)$ and $\left(n+\frac{1}{2}\right)$ points to mid increment values. The central difference integration operator is explicit in that the kinematic state can be advanced using known values from previous increment. Explicit integration is conditionally stable, and is bounded with the following limits:

$$\Delta t \leq \frac{2}{\omega_{\max}} \qquad (5)$$

where $\omega_{\max}$ is the maximum frequency of the system. Explicit method generally implements lumped mass matrix for solving acceleration expediently, therefore eliminating the prerequisite for solving simultaneous sets of equation. This uncouples the equation system such that the equations can be solved on element-to-element basis and there is no need of global matrices, consequently causing a significant minimization of the computation time. An explicit dynamic analysis therefore is very efficient for computation purpose. It is not only proficient for analysis of large models with high-speed dynamic conditions but can also simulate complicated contact conditions. The explicit integration scheme is conditionally stable and should be carefully integrated with small time increments. Abaqus/Explicit uses an adaptive algorithm to determine conservative bounds for the highest element frequency. An estimate of the highest eigenvalue in the system can be obtained by determining the maximum element dilatational mode of the mesh. The stability limit based upon this highest element frequency is conservative in that it will give a smaller stable time increment than the true stability limit that is based upon the maximum frequency of the entire model. Abaqus/Explicit contains a global estimation algorithm, which determines the maximum frequency of the entire model. At the beginning of the analysis, the program evaluates the time step size based on element by element estimation. As the step proceeds, the stability limit will be determined from the global estimator once the algorithm determines that the accuracy of the global estimation is acceptable (Shirole et al., 2017).

III. FINITE ELEMENT MODELING

1. The Equation of Energy and Hugoniot Curve

The equation for conservation of energy equates the increase in internal energy per unit mass, E_m, to the rate at which work is being done by stresses and the rate at which heat is being added.
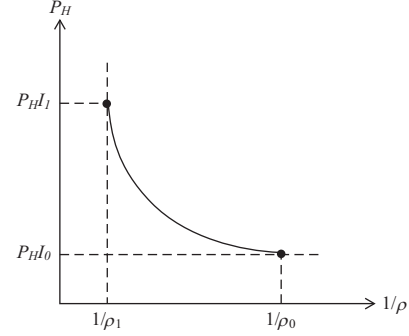

Fig. 1. Schematic representation of a Hugoniot curve (Isbell et al., 1968).

In the absence of heat conduction, the energy equation can be written as Eq. (6):

$$\rho \frac{\partial E_m}{\partial t} = \left(p - p_{bv}\right)\frac{1}{\rho}\frac{\partial \rho}{\partial t} + s : \dot{e} + \rho \dot{Q} \qquad (6)$$

where p is the pressure stress defined as positive in compression, p_{bv} is the pressure stress due to the bulk viscosity, s is the deviator stress tensor, $\dot{e}$ is the deviator part of strain rate, and $\dot{Q}$ is the heat rate per unit mass. According to Abaqus documentation, flow modeling of compressible fluid can be achieved using the linear U_s-U_p form of the Mie-Gruneisen equation of state. The equation of state assumes pressure as a function of the current density, ρ, and the internal energy per unit mass, E_m, according to Eq. (7):

$$p = f\left(\rho, E_m\right) \qquad (7)$$

which defines all the equilibrium states that can exist in a material. The internal energy can be eliminated from Eq. (33), to obtain a pressure (p) vs. volume (V) relationship or, equivalently, a p vs. $1/\rho$ relationship that is unique to the material described by the equation of state model. This equation is uniquely dependent on the material defined by the equation of state. This unique relationship is called the Hugoniot curve and it is the locus of p-V states achievable behind a shock. The Hugoniot pressure, p_H, is only a function of density and can be defined, in general, from fitting experimental data. An equation of state is said to be linear in energy when it can be written as Eq. (8):

$$p = f + gE_m \qquad (8)$$

where $f(\rho)$ and $g(\rho)$ are only functions of density and depend on the particular equation of state model. Fig. 1 shows a schematic expression of a Hugoniot curve (Isbell et al., 1968).

2. Mie-Gruneisen Equation of State

As mentioned previously, an equation of state is used to express the behaviour of Eulerian materials. For a Mie-Gruneisen equation of state for linear energy, the most common form is written as Eq. (9) (Erfanian and Moghiman, 2015):

$$p - p_H = \Gamma \rho \left(E_m - E_H\right) \qquad (9)$$

where p_H and E_H are the Hugoniot pressure and specific energy (per unit mass) and are only functions of density, and Γ is the Gruneisen ratio defined as Eq. (10):

$$\Gamma = \Gamma_0 \frac{\rho_0}{\rho} \tag{10}$$

where Γ_0 is a material constant and ρ_0 is the reference density. Hugoniot energy, E_H, is related to the Hugoniot pressure, p_H, by Eq. (11):

$$E_H = \frac{p_H \eta}{2\rho_0} \tag{11}$$

where η is the nominal volumetric compressive strain, written as Eq. (12):

$$\eta = 1 - \frac{\rho_0}{\rho} \tag{12}$$

Elimination of Γ and E_H, from the above equations yields Eq. (13):

$$p = p_H \left(1 - \frac{\Gamma_0 \eta}{2}\right) + \Gamma_0 \rho_0 E_m \tag{13}$$

The equation of state and the energy equation represent coupled equations for pressure and internal energy. Abaqus solves these equations simultaneously at each material point using an explicit method.

3. Linear U_s-U_p Hugoniot Form

Normally, the U_s-U_p formulation of Equation Of State (EOS) is used to simulate shocks in solid materials. In this study, it is used to define fluid materials. A common fit to the Hugoniot data is given by Eq. (14):

$$p_H = \frac{\rho_0 c_0^2 \eta}{(1 - s\eta)^2} \tag{14}$$

where c_0 and s define the linear relationship between the linear shock velocity, U_s, and the particle velocity, U_p, using Eq. (15):

$$U_s = C_0 + sU_p \tag{15}$$

With the above assumptions the linear U_s-U_p Hugoniot form is written as Eq. (16):

$$p = \frac{\rho_0 c_0^2 \eta}{(1 - s\eta)^2}\left(1 - \frac{\Gamma_0 \eta}{2}\right) + \Gamma_0 \rho_0 E_m \tag{16}$$

where $\rho_0 c_0^2$ is equivalent to the elastic bulk modulus at small nominal strains.

There is a limiting compression given by the denominator of this form of the equation of state. The denominator of Eq. (40)
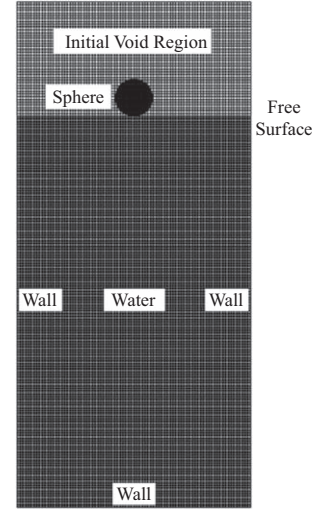

Fig. 2. The computational domain, grid distribution and boundary conditions for the spherical projectile water entry problem.

should not be equal to zero; therefore, an extreme value is defined for ρ and η as Eqs. (17) and (18):

$$\eta_{lim} = \frac{1}{s} \tag{17}$$

$$\rho_{lim} = \frac{s\rho_0}{s-1} \tag{18}$$

At this limit there is a tensile minimum; thereafter, negative sound speeds are calculated for the material. The linear Hugoniot form U_s-U_p equation of state can be employed to model laminar viscous flow governed by the Navier-Stocks equations. The volumetric response is governed by the equations of state, where the bulk modulus acts as a penalty para-meter for the constraint (Erfanian and Moghiman, 2015). The Eulerian part (water) is simulated using the linear U_s-U_p Hugoniot form of the Mie-Gruneisen equation of state.

IV. VALIDATION

Before simulating the water entry problem of the spherical projectile, the accuracy of the numerical model was investigated by comparing the numerical results with the experimental data of Aristoff et al. (2010) for the water entry of a sphere. Fig. 2 shows a schematic of the computational domain, grid distribution and boundary conditions considered for the spherical projectile water entry problem. The dimensions of the computational domain have been chosen large enough, and grid size was gradually decreased until no considerable changes were observed in the numerical results. The spherical projectile was modeled as Lagrangian solid geometry using 15000 mesh elements and a rigid body constraint was applied to it. The Eulerian domain (water) was modeled using quarter symmetry as a cube with dimensions of $30 \times 50 \times 60$ cm^3 and 746172 mesh elements. The Eulerian domain was divided into upper and lower parts. At the initial

Table 1. Equation of state (EOS) parameters for Eulerian domain (water).

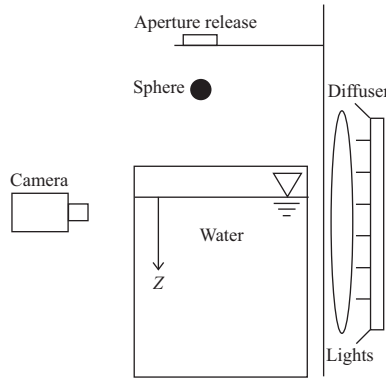| Density (ρ) (kg/m^3)	Dynamic Viscosity (μ) (kgs/m^2)	Sound Velocity (C_0) (m/sec)	Γ	S
1000	0.001	1450	0	0

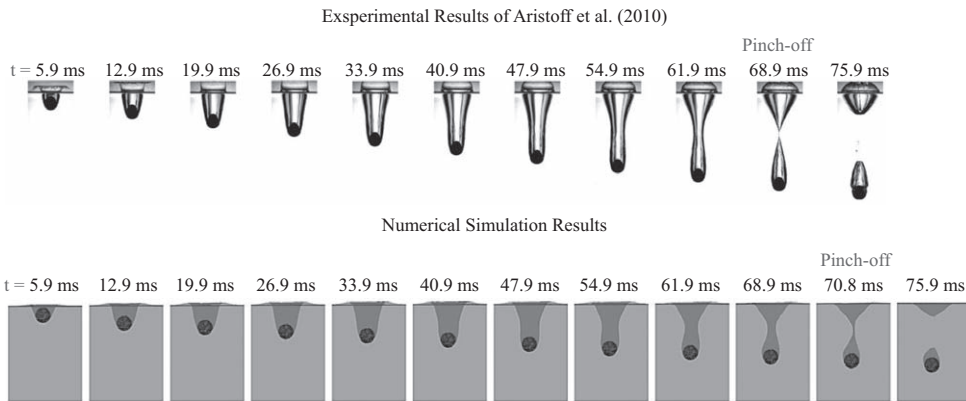**Fig. 3. Schematic of the experimental equipment of Aristoff et al. (2010).**

Fig. 4. Comparison of numerical results with experimental photographs of Aristoff et al. (2010) for the spherical projectile water entry problem.

time ($t = 0$), the upper part was defined as a void and the lower part was defined as stationary water. The diameter of the spherical projectile was 2.54 cm and an initial velocity of 2.17 m/s in the normal direction to the free water surface was applied to it. The spherical projectile can move freely in all directions with six degrees of freedom. The Equation of state (EOS) parameters for Eulerian domain (water) are given in Table 1.
where Γ is material constant in Gruneisen equation of state and S is constant coefficient in shock velocity equation.

Fig. 3 shows a schematic of experimental equipment of Aristoff et al. (2010). A spherical projectile was held at a height h above an experimental tank with dimensions of $30 \times 50 \times 60$ cm^3. Tank was illuminated by a collection of twenty 32-W fluorescent bulbs to improve the high-speed photography and a diffuser was used to provide uniform lighting. The spherical projectile was released from rest and fell towards the water and impacting it with velocity of 2.17 m/s. After entering the water, its deep-water movement was recorded using a high-speed camera at 2000 fps. The camera resolution was set to 524×1280 pixels with a field of view of 11.28×27.55 cm^2, yielding a 46.46 px/cm mag-

nification. The trajectory of the spherical projectile and its impact speed was determined with subpixel accuracy through a cross correlation and Gaussian peak-fitting method yielding position estimates accurate to 0.025 px (0.0005 cm) and impact speeds accurate to $\pm 4\%$.

Fig. 4 shows a comparison of cavity shapes between the experimental photographs taken by Aristoff et al. (2010) and numerical simulation results for a similar period of time. As can be seen, the experimental observations and numerical results are in good agreement and cavity shapes are the same for both experimental and numerical simulation at similar times, except that cavity shape for the pinch-off time of the numerical simulation was added to the pictures.

A symmetric air cavity formed behind the spherical projectile after entering the water. Air cavity formation consists of several steps including cavity creation, cavity expansion, cavity contraction behind the spherical projectile, and cavity collapse. As the spherical projectile moves deeper through the water, it exerts a force on surrounding fluid in radial directions and transfers its momentum to the fluid. However, fluid expansion
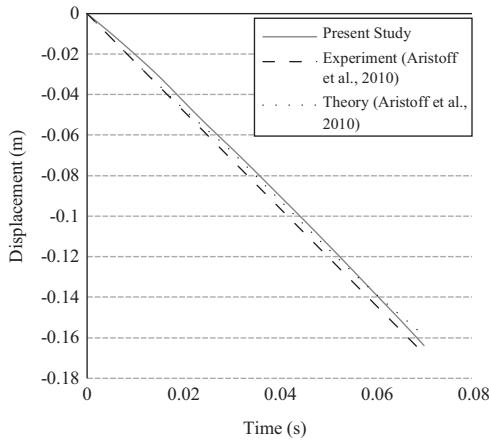
Fig. 5. **Comparison of numerical results for the spherical projectile displacement as a function of time with the theoretical and experimental data of Aristoff et al. (2010).**

Fig. 6. **The computational domain, grid distribution and boundary conditions for water entry problem of spherical projectile.**

Fig. 7. **Comparison of the effect of the Eulerian mesh size on displacement-time graph of spherical projectile.**

is confronted with fluid hydrostatic pressure resistance and as a result, the radial flow direction is reversed, leading to cavity contraction and collapse. Cavity collapse occurs when the cavity wall moves inward until the moment of pinch-off ($t = 70.8$ ms), and the cavity is divided into two separated parts, while the lower cavity sticks to the spherical projectile and moves along with it. The upper cavity then continues its contraction and moves towards the water surface (Taghizadeh-valdi et al., 2018).

Abaqus numerical simulation methods efficiently model water splash and jet flow. Pictures of these phenomena are illustrated in Fig. 4. It was concluded from this figure that pinch-off in the numerical simulation occurs with a delay time compared to the experimental method. Increased numerical errors during solution time is one of the causes for differences between experimental and numerical results.

Fig. 5 shows a comparison of deepwater displacement of spherical projectile as a function of time with the theoretical and experimental data of Aristoff et al. (2010). As can be seen, the numerical results are in a good agreement with those of theoretical and experimental data. However, the presently computed spherical projectile center depth is lower than that found experimentally. It seems that due to lack of turbulent modeling ability in Abaqus Eulerian formulation and evidently increasing turbulence in flow by time, there is only a small difference between experiment and numerical results in the early time of simulation.

V. MATERIAL AND METHODS

1. Eulerian Model Definition

Fig. 6 shows a schematic of the computational domain, grid distribution and boundary conditions for water entry problem of spherical projectile. The dimensions of the computational domain have been chosen large enough, and grid size was gradually decreased until no considerable changes were observed in the numerical results. In water entry problems of rigid bodies, dimensions of the fluid domain must be at least 8 times the dimensio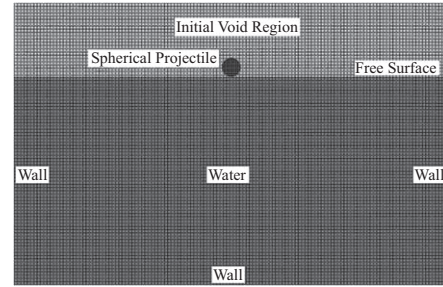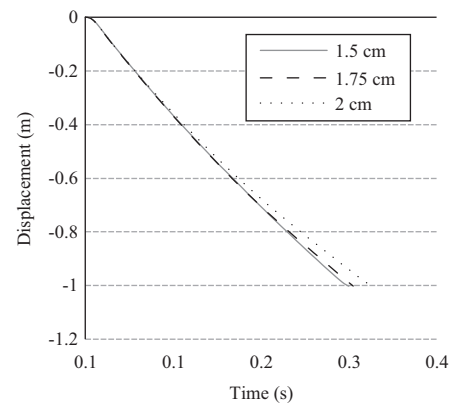ns of the rigid body. The Eulerian domain (water) was modeled using quarter symmetry as a cube with dimensions of $2 \times 2 \times 1$ m^3 and 1538943 mesh elements. Fig. 7 shows a comparison of the effect of the Eulerian mesh size on displacement-time graph of spherical projectile. As can be seen, the graph shows negligible changes for the Eulerian domain mesh size to less than 1.5 cm. The Eulerian domain was divided into upper and lower parts. At the initial time ($t = 0$), the upper part was defined as a void and the lower part was defined as stationary water. The spherical projectile was placed exactly tangent to water surface. An initial velocity in the normal direction to the free water surface was applied to it. The velocity of spherical projectile at the moment of impacting the water surface was determined according to the free fall equation of bodies. Spherical projectile motion in water was not constrained in any direction and it can move freely in all directions with six degrees of freedom. U_s-U_p equation of state was used to define water material in Coupled Eulerian-Lagrangian formulation. This equation of state is useful for Navier-Stokes flow simulation, when the turbulence flow is negligible. In cases where the impact of rigid body on water surface is investigated, the major force imposed on body is the pressure force. Therefore, U_s-U_p equation of state can be used to determine the impact of rigid bodies on water surface (Taghizadeh-valdi et al., 2018).

2. Boundary Condition

For the numerical simulations of water entry problems, a pro-

Table 2. Material properties of spherical projectile.

Material	MassDensity (γ) (kg/m^3)	Young's Modulus (E) (kg/m^2)	Poisson's Ratio (υ)
Steel	7850	2.1×10^{10}	0.3

per artificial computational boundary condition is needed to minimize the reflection of outgoing waves, which can contaminate the fluid domain. This boundary condition is usually called the non-reflecting boundary condition or absorbing boundary condition. The non-reflecting boundaries allows the Eulerian domain to act as a semi-infinite domain, thereby eliminating retransmission waves. In this numerical simulation of water entry problem of spherical projectile, wall boundary conditions was applied to the sides and bottom of computational model and the Eulerian domain boundaries were set as non-reflecting boundaries, so that the waves released due to spherical projectile impact on water surface did not return to the computational domain after reaching these boundaries and being absorbed by them. This boundary condition is written as Eqs. (19) and (20) (Forouzani et al., 2016):

$$dp = pcdu = 0 \qquad (19)$$

$$\frac{dx}{dt} = -c \qquad (20)$$

where ρ is density, c is the speed of sound in fluid, p is pressure, u is velocity perpendicular on wave, and x is the direction perpendicular on the boundary.

3. Lagrangian Model Definition

The spherical projectile with diameter of 10 cm was modeled as Lagrangian solid geometry using 62208 mesh elements and a rigid body constraint was applied to it. In order to reduce analysis time and due to the negligible effect of Lagrangian mesh size on the results, the mesh size for spherical projectile was set to 0.25 cm. Table 2 shows the material properties of the spherical projectile.

4. Drop Height and Impact Velocity of Projectile

After dropping the spherical projectile from a height (h) above the water surface, its impact velocity on water was determined using Eq. (21):

$$V^2 - V_0^2 = 2gh \qquad (21)$$

where V_0 is the projectile initial velocity before being dropped from height h above the water surface, V is projectile secondary velocity at the moment of impacting the water surface, and g is the gravitational acceleration of the Earth.

Eq. (21) is known as a time independent equation for the free fall of bodies, which the initial and terminal velocities of the bodies, drop height, and the gravitational acceleration of the Earth are interdependent on each other in the absence of time. In this numerical simulation, the spherical projectile was dropped from height (h) above the water surface with an initial velocity (V_0) equal to 0 m/s. Therefore, the secondary velocity of

the projectile at the moment of impacting the water surface was determined using Eq. (22):

$$V = \sqrt{2gh} \qquad (22)$$

Instead of simulating a full dropping event from the initial position, the spherical projectile was placed exactly tangent to water surface and its secondary velocity at the moment of impact was obtained according to Eq. (22). A gravitational acceleration (gravity) of -9.8 m/s^2 was assigned to spherical projectile in normal direction.

5. Projectile Motion in Water

For the cavity flows, the liquid phase comes into contact only with the projectile nose. Thus, skin drag can be neglected. Compared with other sources, pressure drag dominates the drag force of a projectile in water. The motion of a projectile with initial velocity v_0 penetrating into a fluid along a trajectory in the $+z$ direction can be described by Newton's second law (Yao et al., 2014):

$$F = m_p \frac{dv_p}{dt} = m_p g - \frac{1}{2} \rho_w A_0 C_d v_p^2 \qquad (23)$$

where m_p is the projectile mass, v_p the penetration velocity of the projectile, F the drag force, A_0 the projected frontal area of the projectile, and C_d is the drag coefficient.

To determine the deepwater displacement and velocity of the spherical projectile in various times, the velocity decay coefficient (β) of the projectile is determined according to Eq. (24) (Yao et al., 2014):

$$\beta = \frac{\pi \rho_w R_0^2 C_d}{2m_p} \qquad (24)$$

where ρ_w is the mass density of water, R_0 is the projectile radius, C_d is the drag coefficient of water and m_p is the projectile mass.

Assuming that C_d is 0.47 for the spherical projectile throughout the water entry process, water mass density is 1000 kg/m^3, projectile radius and mass are 5 cm and 4.11 kg, respectively, and ignoring gravitational effect in the analysis, the deepwater displacement of projectile (Z_p) at different times is obtained according to Eq. (25) (Yao et al., 2014):
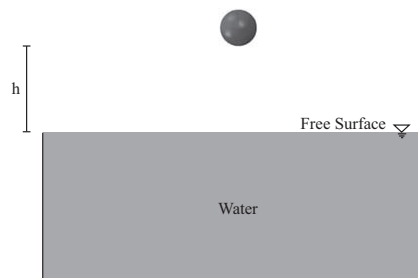
$$Z_p = \frac{1}{\beta} \ln\left(1 + \beta v_0 t\right) \qquad (25)$$

where v_0 is projectile velocity when impacting the water surface and is equal to 4.43 m/s.

In addition, the deepwater velocity of projectile (v_p) at different

Table 3. Velocity of the spherical projectile with different drop heights at the moment of impacting the free water surface.

Drop height of the projectile from free water surface (m)	Projectile velocity at the moment of impacting free water surface (m/s)
0.25	2.21
0.5	3.13
0.75	3.83
1	4.43
1.25	4.95
1.5	5.42
1.75	5.85
2	6.26

Fig. 8. Schematic of drop height of the spherical projectile from free water surface.
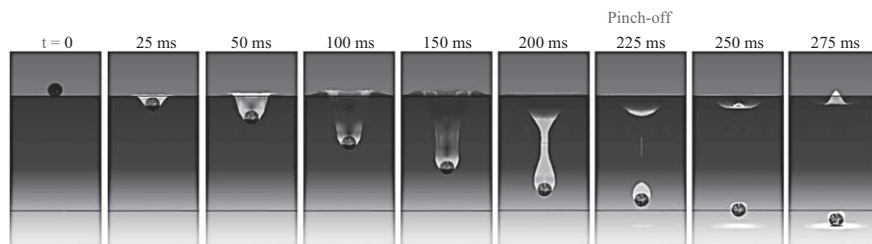
Fig. 9. Air cavity formation due to deepwater movement of spherical projectile and pinch-off time and depth.

times is obtained according to Eq. (26) (Yao et al., 2014):

$$\frac{v_p}{v_0} = \frac{1}{1 + \beta v_0 t} \qquad (26)$$

In this study, the water entry problem of a spherical projectile with different masses of 1 to 6 kg and drop height of 1 m above the free water surface was numerically modeled first, and the effect of increasing the projectile mass on its deepwater displacement, viscous dissipation energy, and pinch-off time and depth was determined. Then, according to Fig. 8, a spherical projectile with a mass of 4.11 kg was dropped from different heights (h), and its velocity at the moment of impacting the water surface was measured according to the time independent equation for free fall of bodies. Table 3 shows the velocity of the spherical projectile with different drop heights at the moment of impacting the water surface. After dropping the spherical projectile from height h above the free water surface with an initial velocity (V_0) of 0 m/s, its velocity gradually increases until it reaches the secondary velocity (V) at the moment of water impact. After entering the water, projectile velocity is decreased due to water drag force. According to time independent equation for the free fall of bodies, increasing the drop height of spherical projectile

from the free water surface leads to increase its secondary velocity at the moment of water surface impact, but it does not necessarily lead to an increase in terminal velocity of projectile at the moment of model bed impact, because the critical drop height of the projectile is a determining factor of its maximum deepwater velocity.

VI. RESULTS AND DISCUSSION

1. Air Cavity Formation and Pinch-Off Time and Depth

Fig. 9 shows the movement trajectory of spherical projectile from the moment of water surface impact to when the projectile reached the model bed. After entering the water, a symmetric air cavity is formed behind the spherical projectile. Air cavity formation involves several steps including air cavity creation and expansion behind the projectile, air cavity contraction, and air cavity collapse. As the spherical projectile moves downward in water depth, it imposes a force onto surrounding fluid in its radial directions and transfers its momentum to the fluid. This extension is faced with the hydrostatic pressure resistance of fluid. The direction of the radial flow is reversed and eventually leads to air cavity contraction and collapse. In other words, the air cavity contraction is accelerated until pinch-off occurs and
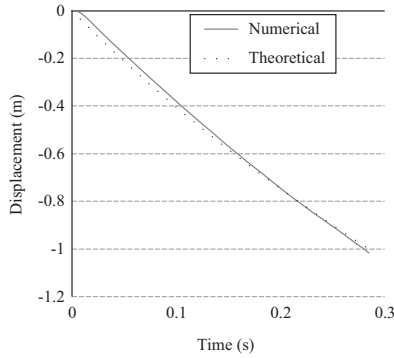
Fig. 10. Comparison of numerical results of spherical projectile displacement in water depth as a function of time with the theoretical results.
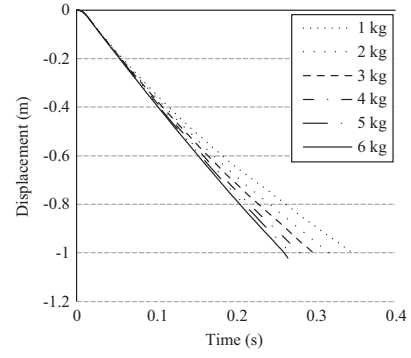

Fig. 11. Comparison of numerical results of spherical projectile velocity in water depth as a function of time with the theoretical results.

Fig. 12. Displacement-time graph of the spherical projectile with different masses.
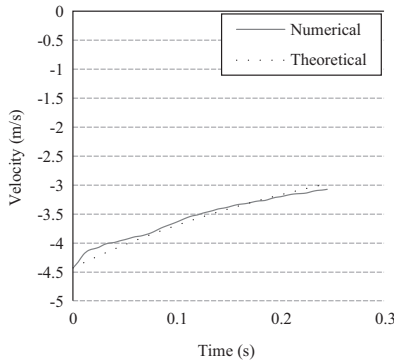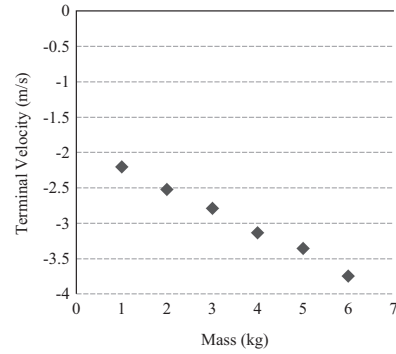

Fig. 13. Terminal velocity vs. mass of spherical projectile.

the air cavity is divided into two distinct parts. The upper part of the air cavity continues its contraction and moves towards the water's surface, whereas the lower part of the air cavity clings to the projectile and moves along with it. The spherical projectile with its curved contact surface has less velocity depreciation. However, some projectile velocity is always depreciated due to impacting the water surface. The velocity depreciation process for the spherical projectile during deepwater movement continues until pinch-off occurs at the time of 225 ms.

The numerical results of spherical projectile displacement and velocity in water depth as functions of time are compared with the theoretical results in Figs. 10 and 11, respectively. As can be seen, the numerical results are well in line with the theoretical results.

2. Effect of Projectile Mass on its Deepwater Displacement

Fig. 12 shows the deepwater displacement-time graphs of spherical projectile with different masses. As can be seen, increasing the projectile mass leads to a decrease in its submersion time from the moment of water surface impact until it reaches the model bed. In fact, increasing the projectile mass results in an increase in its gravitational force (F_g), which is an important factor against the drag force (F_d) of water. On the other hand, the further increase in projectile mass has a subtle effect on deep-

water movement of projectile and submersion time until it reaches the model bed and the displacement-time graphs of the projectile get closer to each other.

3. Effect of Projectile Mass on its Terminal Velocity

Fig. 13 shows the terminal velocity-mass graph of the spherical projectile at the moment of impacting the model bed. As can be seen, increasing the projectile mass leads to an increase in its gravitational force, and results in overcoming the drag force of water, leading to a decrease in its velocity depreciation and subsequently an increase in its terminal velocity when impacting on the model bed.

Figs. 14 and 15 shows the pinch-off time and depth based on the projectile mass, respectively. As can be seen, the pinch-off time is a weak function of the projectile mass and increasing the mass leads to a slight reduction in the pinch-off time, while the pinch-off depth significantly increases along with increased projectile mass.

Fig. 16 shows the viscous dissipation energy-mass graph of the spherical projectile. As can be seen, projectile mass has a subtle effect on energy, and increasing the mass leads to a slight reduction in the viscous dissipation energy.

4. Effect of Projectile Drop Height from Water Surface on its Deepwater Displacement

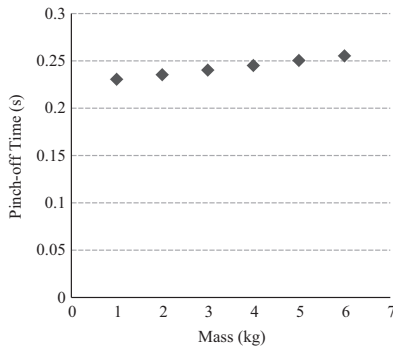Fig. 17 shows the deepwater displacement-time graphs of

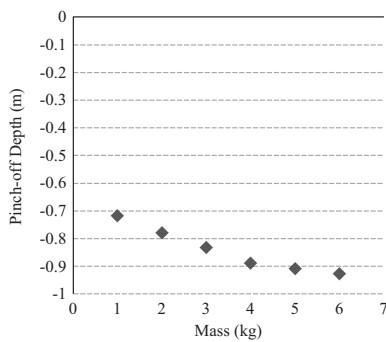**Fig. 14. Pinch-off time vs. mass of spherical projectile.**

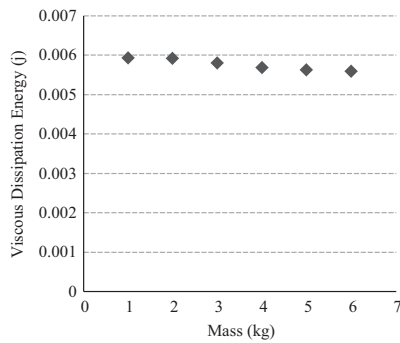**Fig. 15. Pinch-off depth vs. mass of spherical projectile.**

Fig. 16. Viscous dissipation energy vs. mass of spherical projectile.

Fig. 17. Displacement-time graph of the spherical projectile with different drop heights.
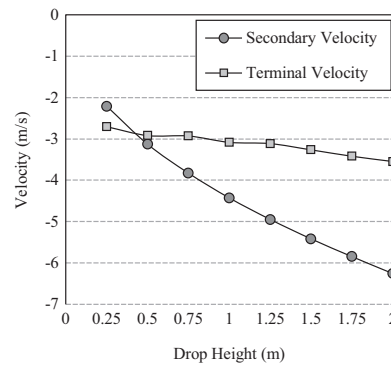
Fig. 18. Secondary and terminal velocities vs. drop heights of spherical projectile.

the spherical projectile with different drop heights from the free water surface. As can be seen, increasing the drop height of the spherical projectile leads to an increase in its secondary velocity when impacting the free water surface and the projectile enters the water with a higher velocity and reaches the model bed in less time. Hence, displacement-time graphs of the spherical projectile get closer to each other.

5. Effect of Projectile Drop Height from Water Surface on its Terminal Velocity

Fig. 18 shows the secondary and terminal velocities of the spherical projectile with different drop heights from the free water surface. When the projectile is dropped from a low height above the free water surface, due to lack of access to high velocity, it moves deepwater due to its mass. Moreover, because
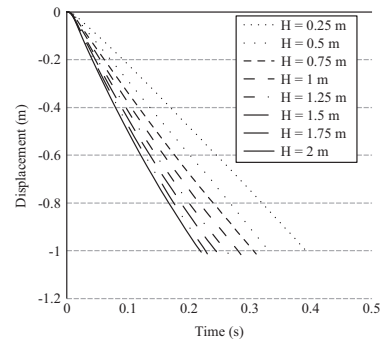
of the low velocity of the projectile when entering the water, the pinch-off occurs in less time and lower depth of water, and its velocity increases after pinch-off till it reaches the terminal velocity. Increasing the drop height of projectile from water surface leads to increasing the difference between the secondary and terminal velocities of the projectile. Hence, it will experience greater velocity depreciation in the first moments of entering water. Increasing the drop height of more than critical drop height leads to increasing the secondary velocity of the projectile when impacting the water surface and decreasing the terminal velocity when impacting the model bed. Hence, the difference between the secondary and terminal velocities of the projectile is not reasonable, and a significant amount of the projectile secondary velocity is depreciated when entering the water.

Figs. 19 and 20 shows the pinch-off time and depth based on the secondary velocity of projectile at the moment of impacting the free water surface, respectively. As can be seen, the pinch-off time is a weak function of the projectile impact velocity and increasing the impact velocity leads to a slight reduction in the pinch-off time, while the pinch-off depth is a linear function of the projectile impact velocity. This behaviour was also observed in the analytical and numerical results found by Lee et al. (1997).

Fig. 21 shows the viscous dissipation energy based on secondary velocity of projectile at the moment of impacting the free water surface. As can be seen, increasing the drop height of the
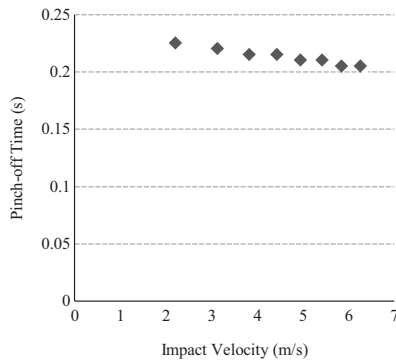
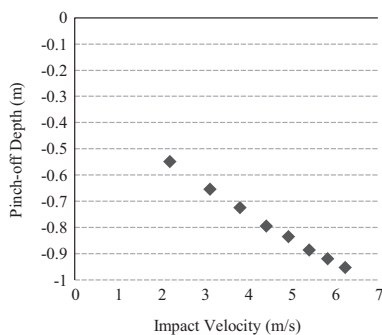**Fig. 19. Pinch-off time vs. impact velocity of spherical projectile.**

Fig. 20. Pinch-off depth vs. impact velocity of spherical projectile.

Fig. 21. Viscous dissipation energy vs. impact velocity of spherical projectile.

spherical projectile above the free water surface leads to a significant decrease in viscous dissipation energy. According to time independent equation for the free fall of bodies, increasing the drop height of spherical projectile from the free water surface leads to increased its secondary velocity at the moment of water surface impact, but after projectile impact on free surface of and entering water, a significant part of projectile velocity is depreciated due to water and leads to viscous energy dissipation.

VII. CONCLUSIONS

In this study, the water entry problem of spherical projectile was numerically simulated by commercial finite element code Abaqus 6.14-2. An explicit dynamic analysis method was employed to model the fluid-structure interactions using a Coupled Eulerian-Lagrangian (CEL) formulation. Before simulating the water entry problem of the spherical projectile, the accuracy of the numerical model is investigated by comparing the numerical results with the experimental data of Aristoff et al. (2010) for the water entry of a sphere. The good agreement between the numerical simulation results with theoretical data and experimental observations found by Aristoff et al. (2010) reveals the accuracy and validity of the employed numerical methodology to simulate the water entry problem of spherical projectile. After dropping the spherical projectile from height of 1 m above the free water surface and entering the water, a symmetric air cavity is formed behind the projectile. As the projectile moves downward in water depth, it imposes a force to surrounding fluid
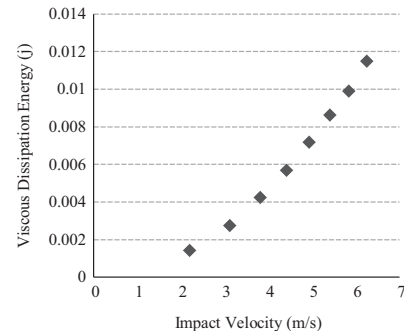
in radial direction and transfers its momentum to fluid. But this extension is faced with hydrostatic pressure resistance of fluid. Then the direction of the radial flow is reversed and eventually leads to air cavity contraction and collapse. The results show that increasing the spherical projectile mass and drop height from free water surface leads to a decrease in its submersion time from the moment of entering the water until it reaches the model bed. In fact, increasing the spherical projectile mass leads to an increase in its gravitational force, and results in overcoming the drag force of water, leading to a decrease in its velocity depreciation and subsequently an increase in its terminal velocity when impacting on the model bed. In contrast, increasing the spherical projectile drop height from free water surface to greater than the critical drop height leads to increase its secondary velocity when impacting the water surface and a decrease in its terminal velocity when impacting the model bed. The pinch-off time is a very weak function of projectile mass and impact velocity on water surface, but the pinch-off depth significantly increases along with increased mass and impact velocity of projectile. Additionally, the projectile mass has a subtle effect on energy, and increasing the mass leads to a slight reduction in the viscous dissipation energy, while increasing the drop height of the spherical projectile above the free water surface leads to a significant decrease in viscous dissipation energy.

ACKNOWLEDGEMENTS

REFERENCES

ABAQUS. (2014) Getting Started with ABAQUS: Interactive Edition. Version 6.14. Dassault Systèmes Simulia Corp., Providence, RI, USA.

Ahmadzadeh, M., B. Saranjam, A. Hoseini-Fard and A. R. Binesh (2014). Numerical simulation of sphere water entry problem using Eulerian-Lagrangian method. Journal of Applied Matheatical Modelling 38, 1673-1684.

Anghileri, M. and A. Spizzica (1995). Experimental validation of finite element models for water impacts. Proceedings of the 2nd international crash users' seminar, Cranfield Impact Centre Ltd, England.

Aristoff, J. M. and J. W. M. Bush (2009). Water entry of small hydrophobic spheres. Journal of Fluid Mechanics 619, 45-78.

Aristoff, J. M., T. T. Truscott, A. H. Techet and J. W. M. Bush (2010). The water entry of decelerating spheres. Physics of Fluids Journal 22(3), 1-8.

Battistin, D. and A. Iafrati (2003). Hydrodynamic loads during water entry of two-dimensional and axisymmetric bodies. Journal of Fluids and Structure 17, 643-664.

Chaung, S. (1966). Slamming of rigid wedge shaped bodies with various deadrise angles. Structural Mechanics Laboratory Research and development, no. 2268.

Engle, A. and R. Lewis (2003). A comparison of hydrodynamic impacts prediction methods with two dimensional drop test data. Journal of Marine Structures 16, 175-182.

Erfanian, M. R. and M. Moghiman (2015). Numerical and experimental investigation of a projectile water entry problem and study of velocity effect on time and depth of pinch-off. Journal of Modares Mechanical Engineering 15, 53-60.

Erfanian, M. R., M. Anbarsooz, N. Rahimi, M. Zare and M. Moghiman (2015). Numerical and experimental investigation of a three dimensional sphericalnose projectile water entry problem. Journal of Ocean Engineering 104, 397-404.

Fairlie-Clarke, A. C. and T. Tveitnes (2007). Momentum and gravity effects during the constant velocity water entry of wedge-shaped sections. Journal of Ocean Engineering 35, 706-716.

Forouzani, H., B. Saranjam, R. Kamali and A. Abdollahi-far (2016). Elastoplastic time dependent impact analysis of high speed projectile on water surface. Journal of Solid and Fluid Mechanics 3, 281-298.

Gilbarg, D. and R. A. Andersok (1948). Influence of atmospheric pressure on the phenomena accompanying the entry of spheres into water. Journal of Applied Physics 19, 127-139.

Glowinski, R., T. W. Pana, T. I. Hesla and D. D. Joseph (1999). A distributed Lagrange multiplier/fictitious domain method for particulate flows. International Journal of Multiphase Flows 25, 755-794.

Goharzadeh, A. and A. Molki (2012). Experimental study of water entry and exit of a circular cylinder at free surface. Proceedings of the ASME 2012 International Mechanical Engineering Congress and Exposition, Texas, USA.

Hafsia, Z., C. Mnasri, O. Mohamed and K. Maalel (2009). Water entry and exit of horizontal cylinder in free surface flow. Proceedings of the International Symposium on Convective Heat and Mass Transfer in Sustainable Energy, Tunisia, April 26.

Howison, S. D., J. R. Ockendon and S. K. Wilson (1991). Incompressible waterentry problems at small deadrise angles. Journal of Fluid Mechanics 222, 215-230.

Iranmanesh, A. and M. Passandideh-Fard (2017). A three-dimensional numerical approach on water entry of a horizontal circular cylinder using the volume of fluid technique Ocean Engineering 130, 557–566.

Isbell, W. M., F. H. Shipman and A. H. Jones (1968). Hugoniot equation of state measurements for eleven material to five megabars materials and structural laboratory manufacturing developments. General Motors Technical center, Michigan, USA.

Kim, S. and N. Kim (2015). Integrated dynamics modeling for supercavitating vehicle systems. International Journal of Naval Architecture and Ocean Engineering 7, 346-363.

Kim, Y. W., Y. Kim, Y. M. Liu and D. Yue (2007). On the water-entry impact problem of asymetric bodies. Proceedings of 9th International Conference on Numerical Ship Hydrodynamics, Michigan, USA.

Kleefsman, K. M. T., G. Fekken, A. E. P. Veldmen, B. Lwanowski and B. Buchner (2005). A volume of fluid based simulation method for wave impact problems. Journal of Computational Physics 206, 363-393.

Korobkin, A. A. and M. Ohkusu (2004). Impact of two circular plates one of which is floating on a thin layer of liquid. Journal of Engineering Mathematics 50, 343-358.

Lee, M., R. G. Longoria and D. E. Wilson (1997). Cavity dynamics in high-speed water entry. Physics of Fluids 9, 541-550.

May, A. (1951). Effect of surface condition of a sphere on its water-entry cavity. Journal of Applied Physics 22, 1219-1222.

May, A. (1952). Vertical entry of missiles into water. Journal of Applied Physics 23, 1362-1372.

May, A. and J. C. Woodhull (1948). Drag coefficients of steel spheres entering water vertically. Journal of Applied Physics 19, 1109-1121.

Miloh, T. (1991). On the initial stage slamming of a rigid sphere in a vertical water entry. Journal of Applied Ocean Research 8, 13-43.

Mirzaei, M., M. Eghtesad and M. M. Alishahi (2016). Planing force identification in high-speed underwater vehicles. Journal of Vibration and Control 22, 4176-4191.

Mirzaii, I. and M. Passandideh-Fard (2012). Modeling free surface flows in presence of an arbitrary moving object. International Journal of Multiphase Flows 39, 216-226.

Moghisi, M. and P. T. Squire (1981). An experimental investigation of the initial force of impact on a sphere striking a liquid surface. Journal of Fluid Mechanics 108, 133-146.

New, A. P., T. S. Lee and H. T. Low (1993). Impact loading and water entrance characteristics of prismatic bodies. Proceedings of the 3th international offshore and polar engineering conference, National University of Singapore, Singapore, pp. 282-287.

Nguyen, V. T., D. T, Vu, W. G. Park and Y. R, Jung (2014). Numerical analysis of water impact forces using a dual-time pseudo-compressibility method and volume-of-fluid interface tracking algorithm. Computer and Fluids 103, 18-33.

Nguyen, V. T., D. T. Vu, W. G. Park and C. M. Jung (2016). Navier-Stokes solver for water entry bodies with moving Chimera grid method in 6DOF motions. Computers and Fluids 140, 19-38.

Park, M., Y. Jung and W. Park (2003). Numerical study of the impact force and ricochet behaviour of high speed water entry bodies. Computer Fluids Journal 51, 932-939.

Shirole, D., C. Moormann and K. G. Sharma (2017). A new continuum based model for the simulation of a seismically induced large-scale rockslide. Journal of Procedia Engineering 173, 1755-1762.

Szebehely, V. G. (1959). Hydrodynamic impact. Journal of Applied Mechanics 12, 297-300.

Taghizadeh-Valdi, M. H., M. R. Atrechian, A. Jafary Shalkoohy and E. Chavoshi (2018), Numerical Investigation of Water Entry Problem of Pounders with Different Geometric Shapes and Drop Heights for Dynamic Compaction of Seabed. Geofluids 2018 (4), 1-18.

Tassin, A., D. J. Piro, A. A. Korobkin, K. J. Maki and M. J. Cooker (2013). Two-dimensional water entry and exit of a body whose shape varies in time. Journal of Fluid Structure 40, 317–336.

Techet, A. H. and T. T. Truscott (2011). Water entry of spinning hydrophobic and hydrophilic spheres. Journal of Fluids and Structures 27, 716-726.

Truscott, T. T., B. P. Epps and J. Belden (2014). Water entry of projectiles. Annual Review of Fluid Mechanics 46, 355-378.

Von Karman, T. (1929). The impact of seaplane floats during landing. National Advisory Committee for Aeronautics, NACA TN, no. 321.

Wagner, H. (1932). Phenomena associated with impacts and sliding on liquid surfaces. Journal of Applied Mathematics and Mechanics 12, 193-215.

Watanabe, S. (1930). Resistance of impact on water surface, part I-cone. Institute of Physical and Chemical Research, Tokyo 12, 251-267.

Watanabe, S. (1930). Resistance of impact on water surface, part II-cone (continued). Institute of Physical and Chemical Research, Tokyo 14, 153-168.

Watanabe, S. (1934). Resistance of impact on water surface. Part V-sphere. Scientific papers of the Institute of Physical and Chemical Research 484, 202-208.

Worthington, A. M. (1908). A Study of Splashes. Longmans, Green, and Co, London.

Worthington, A. M. and A. M. Cole (1897). Impact with a liquid studied by the aid of instantaneous photography. Philosophical Transactions of the Royal Society A 189, 137–1480.

Wu, G. (2012). Numerical simulation for water entry of a wedge at varying speed by a high order boundary element method. Journal of Marine Science and Application 11(2), 143-149.

Yang, Q. and W. Qiu (2007). Numerical solution of 2D slamming problem with a CIP method. International Conference on Violent Flows, Research Institute for Applied Mechanics, Kyushu University, Japan.

Yang, Q. and W. Qiu (2012). Numerical simulation of water impact for 2D and 3D bodies. Journal of Ocean Engineering 43, 82-89.

Yao, E., H. Wang, P. Long, X. Wang and R. Woding (2014). Vertical water-entry of bullet-shaped projectiles. Journal of Applied Mathematics and Physics 2, 323-334.

Zhu, X., O. M. Faltinsen and C. Hu (2006). Water entry and exit of a horizontal circular cylinder. Journal of Offshore Mechanics and Arctic Engineering 129, 253-264.